

# Giant negative thermal expansion exceeding 1000 K in PrMnO<sub>3</sub> via synergy of local structure distortion and orbital disordering

Received: 7 March 2025

Accepted: 26 September 2025

Published online: 13 November 2025

Check for updates

Feiyu Qin<sup>1</sup>✉, Xiaoya Bai<sup>1</sup>, Yue-Wen Fang<sup>2,3</sup>, Pengli Zhu<sup>4</sup>, Jun Wang<sup>5</sup>, Pengtao Cheng<sup>6</sup>✉, Dunhui Wang<sup>6</sup>, Lei Hu<sup>1</sup>✉, Jun Sun<sup>1</sup> & Xiangdong Ding<sup>1</sup>

Giant negative thermal expansion (NTE), defined by volumetric expansion  $\alpha_V < \text{ca. } -50 \times 10^{-6} \text{ K}^{-1}$  (volume contraction ( $\Delta V/V < -0.5\%$  within  $\sim 100$  K), is rarely observed at high temperatures. Here, we report a giant NTE persisting above 1000 K ( $\Delta V/V = -1.7\%$ , 900–1100 K) in stoichiometric PrMnO<sub>3</sub> (PMON) with a peak coefficient  $\alpha_V = -114 \times 10^{-6} \text{ K}^{-1}$  around 1000 K. Contrastingly, oxygen-rich PrMnO<sub>3+x</sub> (PMOA) exhibits only positive thermal expansion. The origin of NTE was uncovered via synchrotron X-ray total scattering, Cs-corrected STEM, and DFT calculations. Intriguingly, PMON uniquely hosts a local symmetry breaking featured by a 3D cross-arranged network of elongated Mn-O bonds, different from the 2D planar configurations in PMOA. By correlating atomic-scale symmetry breaking and thermally activated orbital reconfiguration to macroscopic thermal responses, we establish an unconventional paradigm for engineering giant NTE at elevated temperatures.

Materials with colossal negative thermal expansion (NTE) at elevated temperatures show exceptional promise in mitigating thermo-mechanical instability faced by high-temperature components, including engine turbine blades, thermal barrier coatings, and thermal management systems<sup>1,2</sup>. Nevertheless, materials demonstrating substantial lattice contraction with giant NTE coefficients remain scarce, particularly in high-temperature regimes ( $>500$  K). NTE phenomenon arises from diverse physical mechanisms, such as geometric flexibility in framework compounds<sup>3–5</sup>, ferroelectric and magnetic phase transition<sup>6,7</sup>, charge (or orbital) ordering transition<sup>8–11</sup>, etc. These mechanisms counteract the positive thermal expansion (PTE) induced by high-frequency phonon modes<sup>12</sup>. As temperature increases, high-frequency phonon overwhelmingly prevails, resulting in severe constraints: most giant NTEs are confined to modest temperature ranges (typically  $<500$  K) with limited magnitude of volume contraction.

The pursuit of giant NTE materials and their governing mechanisms remains an active frontier<sup>13–17</sup>. Electron-driven mechanisms,

particularly those involving charge transfer, orbital reconfiguration, and ferroelectric/magnetic phase transitions, have emerged as critical pathways for achieving pronounced NTE. For instance, Bi<sub>0.95</sub>La<sub>0.05</sub>NiO<sub>3</sub> demonstrates a  $-2.9\%$  lattice volume shrinkage ( $\Delta V/V$ ) between 300–370 K with  $\alpha_V = -413 \times 10^{-6} \text{ K}^{-1}$  via charge transfer<sup>8</sup>. (Sm, Y)S single crystal exhibits  $\alpha_V = -195 \times 10^{-6} \text{ K}^{-1}$  (100–315 K)<sup>18</sup>. Pb<sub>0.7</sub>Bi<sub>0.3</sub>VO<sub>3</sub> undergoes a  $-7.9\%$  volume reduction (550–800 K) through ferroelectric phase transitions<sup>19</sup>. Orbital ordering (OO) induced NTE in Ca<sub>2</sub>RuO<sub>4-x</sub> yields a  $-1\%$  volume reduction with  $\alpha_V = -48 \times 10^{-6} \text{ K}^{-1}$  (135–345 K)<sup>9</sup>. Additional materials like Mn(Co, Cr)Ge ( $\alpha_V = -155 \times 10^{-6} \text{ K}^{-1}$ , 122–332 K)<sup>20</sup>, (Ni, Fe)S ( $\alpha_V = -293 \times 10^{-6} \text{ K}^{-1}$ , 240–290 K)<sup>21</sup>, La(Fe, Co, Si)<sub>13</sub> ( $\alpha_V = -78 \times 10^{-6} \text{ K}^{-1}$ , 240–350 K)<sup>7</sup> further underscore the prevalence of electron-driven NTE. By far, electron-driven type NTEs predominantly operate below 500 K, necessitating strategies to extend their operational windows to higher temperatures<sup>22,23</sup>. In contrast, low-frequency phonon driven NTE materials (e.g., framework compounds) exhibit a relatively wide

<sup>1</sup>State Key Laboratory for Mechanical Behavior of Materials, Xi'an Jiaotong University, Xi'an, China. <sup>2</sup>Fisika Aplikatua Saila, Gipuzkoako Ingeniaritza Eskola, University of the Basque Country (UPV/EHU), Europa Plaza 1, Donostia San Sebastian, Spain. <sup>3</sup>Centro de Física de Materiales (CFM-MPC), CSIC-UPV/EHU, Manuel de Lardizabal pasealekua 5, Donostia/San Sebastián, Spain. <sup>4</sup>Shenzhen Institute of Advanced Electronic Materials, Shenzhen Institute of Advanced Technology, Chinese Academy of Sciences, Shenzhen, China. <sup>5</sup>Department of Materials Science, Fudan University, Shanghai, China. <sup>6</sup>Hangzhou Dianzi University, Hangzhou, Zhejiang, China. ✉e-mail: feiyu\_qin@xjtu.edu.cn; cpt@hdu.edu.cn; leihu@xjtu.edu.cn

temperature window that may eventually expand into the high-temperature range<sup>24</sup>, but suffer from diminished contraction magnitudes at elevated temperatures: ScF<sub>3</sub> displays  $\alpha_v = -14.1 \times 10^{-6} \text{ K}^{-1}$  (10–1100 K,  $\Delta V/V \approx -1.5\%$ ), yet its contraction attenuates to  $-0.05\%$  near 1000 K ( $\alpha_v = -2.1 \times 10^{-6} \text{ K}^{-1}$ , 760–1000 K). NaB(CN)<sub>4</sub> shows  $\alpha_v$  degradation from  $-92 \times 10^{-6} \text{ K}^{-1}$  (100–200 K) to  $-36 \times 10^{-6} \text{ K}^{-1}$  at  $-650 \text{ K}$ <sup>25</sup>. Notably, as far as we know, no material has demonstrated giant NTE ( $\alpha_v < -100 \times 10^{-6} \text{ K}^{-1}$ ) beyond 1000 K, highlighting a critical gap in high-temperature NTE engineering.

Perovskite-type RMnO<sub>3</sub> (R = rare earth elements), characterized by the Jahn-Teller (JT) distortion of Mn<sup>3+</sup> cations, have attracted multidisciplinary interest in catalysis, energy conversion/storage, magnetic recording, and electromagnetic wave absorption due to their unique electronic and magnetic functionalities<sup>26–29</sup>. Within this family, LaMnO<sub>3</sub>—the parent compound exhibiting colossal magnetoresistance—has been extensively studied through chemical doping at R/Mn sites and oxygen stoichiometry modulation<sup>30</sup>. These investigations focus on elucidating the interplay between crystal structure evolution, JT transitions, electronic configurations, and OO, aiming to decode the origins of its extraordinary properties<sup>31–33</sup>. Specifically, orbital order-disorder transitions (OO to OD) and localized JT distortions in LaMnO<sub>3</sub> give clues to the origin of its  $-0.36\%$  volume collapse between 720–750 K<sup>34</sup>. Similarly, PrMnO<sub>3</sub> demonstrates an anomalous  $-0.1\%$  lattice contraction near 200–300 K<sup>35</sup>. Notably, neutron diffraction investigation on PrMnO<sub>3</sub> observed thermal shrinkage aligns with our NTE framework<sup>36</sup>, while established phase diagrams inform oxygen stoichiometry design strategies<sup>37</sup>. These observations highlight the potential of RMnO<sub>3</sub> perovskites as candidates for high-*T* giant NTE.

In this work, we report a breakthrough in achieving giant NTE above 1000 K through oxygen stoichiometry engineering in PrMnO<sub>3</sub>. Specifically, stoichiometric PrMnO<sub>3</sub> (PMON) exhibits a colossal volume contraction exceeding 1000 K ( $\Delta V/V = -1.7\%$ , 900–1100 K) with a peak volumetric thermal expansion coefficient  $\alpha_v = -114 \times 10^{-6} \text{ K}^{-1}$  around 1000 K. In contrast, oxygen-excess PrMnO<sub>3+x</sub> (PMOA) displays conventional PTE. The electronic structure analysis was performed via X-ray absorption spectroscopy (Mn K-, O K-, and Mn L-edges). Temperature-dependent synchrotron X-ray diffraction (SXRD) unveiled dynamic MnO<sub>6</sub> octahedral geometry changes and JT distortion evolution. Pair distribution function analysis (PDF) and aberration-corrected scanning transmission electron microscopy (STEM) revealed a unique local structural distortion in PMON, characterized by three-dimensional (3D) cross-arrangement of elongated Mn–O bonds and zigzag atomic configurations. Conversely, PMOA adopts a two-dimensional planar distribution of elongated Mn–O bond. The first-principles density functional theory (DFT) calculations give electronic orbital patterns and JT distortion in degree of PMON-derived structural models, revealing condition-dependent orbital evolution pathways. This study establishes the highest-temperature giant NTE reported to date and pioneers a strategic pathway for tailoring anomalous thermal expansion through manipulating oxygen stoichiometry.

## Results and discussion

### Electronic structure analysis and NTE

PrMnO<sub>3</sub> with excess lattice oxygen (denoted as PMOA) was synthesized via a solid-state reaction under the ambient atmosphere. Stoichiometric PrMnO<sub>3</sub> (designated as PMON) was obtained through citrate precursor decomposition followed by nitrogen-atmosphere annealing to remove oxygen excess. Figure 1a displays synchrotron X-ray diffraction (SXRD) patterns of PMOA and PMON at 800 K, with characteristic reflections indexed to the orthorhombic *Pnma* structure.

To probe the electronic structures of PMON and PMOA, we present O K-edge and Mn L-edge XAS spectra for both compounds alongside reference standards (Mn<sub>2</sub>O<sub>3</sub> and MnO<sub>2</sub>) in Fig. 1b, c. Three characteristic features (denoted A, B, C) emerge in PMON and PMOA,

ascribed to hybridized states of O 2*p*-Mn 3*d*, O 2*p*-Pr 5*d*, and O 2*p*-Mn 4*sp* respectively<sup>38</sup>. The O K-edge spectra of both materials exhibit close resemblance to Mn<sub>2</sub>O<sub>3</sub> but distinct divergence from MnO<sub>2</sub>. Critically, the pre-edge feature (A) below 535 eV corresponds to unoccupied O 2*p*-Mn 3*d* hybridized states<sup>39</sup>, whose intensity correlates directly with Mn valence—a relationship established in analogous systems like (La, Sr)MnO<sub>3</sub> where enhanced pre-edge intensity accompanies hole doping and elevated Mn oxidation states<sup>40</sup>. Notably, the markedly intensified pre-edge feature in PMOA (indicated by the black arrow, Fig. 1b) relative to PMON provides direct spectroscopic evidence of a higher Mn valence in PMOA.

The Mn L-edge XAS spectra exhibit characteristic L<sub>3</sub> (2*p*<sub>3/2</sub>) and L<sub>2</sub> (2*p*<sub>1/2</sub>) peaks arising from spin-orbit coupling, as shown in Fig. 1c. PMON displays peak profiles and positions closely resembling Mn<sub>2</sub>O<sub>3</sub> (Mn<sup>3+</sup>), particularly evident in the identical L<sub>3</sub>-edge maximum (black bar). While PMOA maintains this L<sub>3</sub>-edge maximum, a distinct high-energy shoulder (violet dotted line) aligns with the L<sub>3</sub>-edge peak of MnO<sub>2</sub>, suggesting an average Mn valence exceeding +3. The dominant Mn<sup>3+</sup> valence state, admixed with minor Mn<sup>4+</sup>, aligns with X-ray photoelectron spectroscopy (XPS) data (Fig. S2). Further supporting this, the L<sub>2</sub>-edge maximum for PMON occurs at 652.8 eV—identical to Mn<sub>2</sub>O<sub>3</sub>—whereas PMOA shows a slight shift to 652.9 eV. Both values remain significantly lower than MnO<sub>2</sub>'s 653.4 eV. This systematic L<sub>2</sub>-edge blueshift is analogous to observations in La<sub>1-x</sub>Sr<sub>x</sub>MnO<sub>3</sub> systems, where valence increases from +3 (652.2 eV) to +3.9 (653.0 eV)<sup>40</sup>. Collectively, these features indicate a +3 valence state for PMON, analogous to Mn<sub>2</sub>O<sub>3</sub>, while PMOA exhibits a slightly elevated valence consistent with charge compensation via oxygen incorporation. Moreover, we systematically analyzed the first derivatives of the Mn K-edge X-ray absorption near-edge structure spectra (Fig. S1b), yielding estimated valences of +3 for PMON and +3.16 for PMOA. These values align with XPS and Raman spectroscopy analyses (Figs. S2, 3). Charge compensation considerations further indicate an oxygen stoichiometry of PrMnO<sub>3.08</sub> for PMOA.

Temperature-dependent SXRD profiles of PMOA and PMON were analyzed via Rietveld refinement using the orthorhombic *Pnma* structural model (Fig. S2). Figure 1d illustrates the thermal evolution of characteristic diffraction peaks. PMON exhibits merging of (110) and (002) reflections near 1000 K, corresponding to an orthorhombic-to-orthorhombic structural phase transition. Distinct thermal responses are observed: PMOA peaks systematically shift to lower 2θ angles with heating, whereas PMON peaks above 1000 K migrate toward higher angles, reflecting divergent thermal expansion properties in PMOA and PMON. Indeed, quantitative analysis (Fig. 1e) demonstrates conventional PTE in PMOA (blue hexagon), with an average volumetric coefficient  $\alpha_v = 32 \times 10^{-6} \text{ K}^{-1}$  (800–1100 K). Lattice parameters *a*, *b*, and *c* monotonically increase with temperature (Fig. S3a–c). In stark contrast, PMON displays giant NTE, achieving the peak  $\alpha_v = -114 \times 10^{-6} \text{ K}^{-1}$  around 1000 K. A  $-1.7\%$  volume contraction occurs between 900–1100 K (average  $\alpha_v = -85 \times 10^{-6} \text{ K}^{-1}$ ), surpassing the reported colossal NTE systems mediated by charge transfer (CT), magnetic ordering (MO), phonon (PH), or orbital-ordering (OO) mechanisms (Fig. 1f). Notably, PMON demonstrates operational stability for colossal NTE, maintaining functionality above 1000 K—the highest temperature window reported to date.

The reversibility and reproducibility of the giant NTE and PTE in PMON and PMOA are rigorously confirmed by SXRD and laboratory-based XRD measurements, as illustrated in Fig. S6–9. Moreover, the Mn L-edge XAS spectra of PMON and PMOA, which were after high-temperature X-ray experiment, retain spectral features identical to the reference Mn<sub>2</sub>O<sub>3</sub>, as detailed in Fig. S10. This spectral invariance effectively excludes manganese oxidation as a contributory mechanism for the observed lattice volume contraction. The observed difference in peak maxima of the Mn L edge of Mn<sub>2</sub>O<sub>3</sub> between Figs. 1c, S10 aligns with well-established knowledge of systematic energy

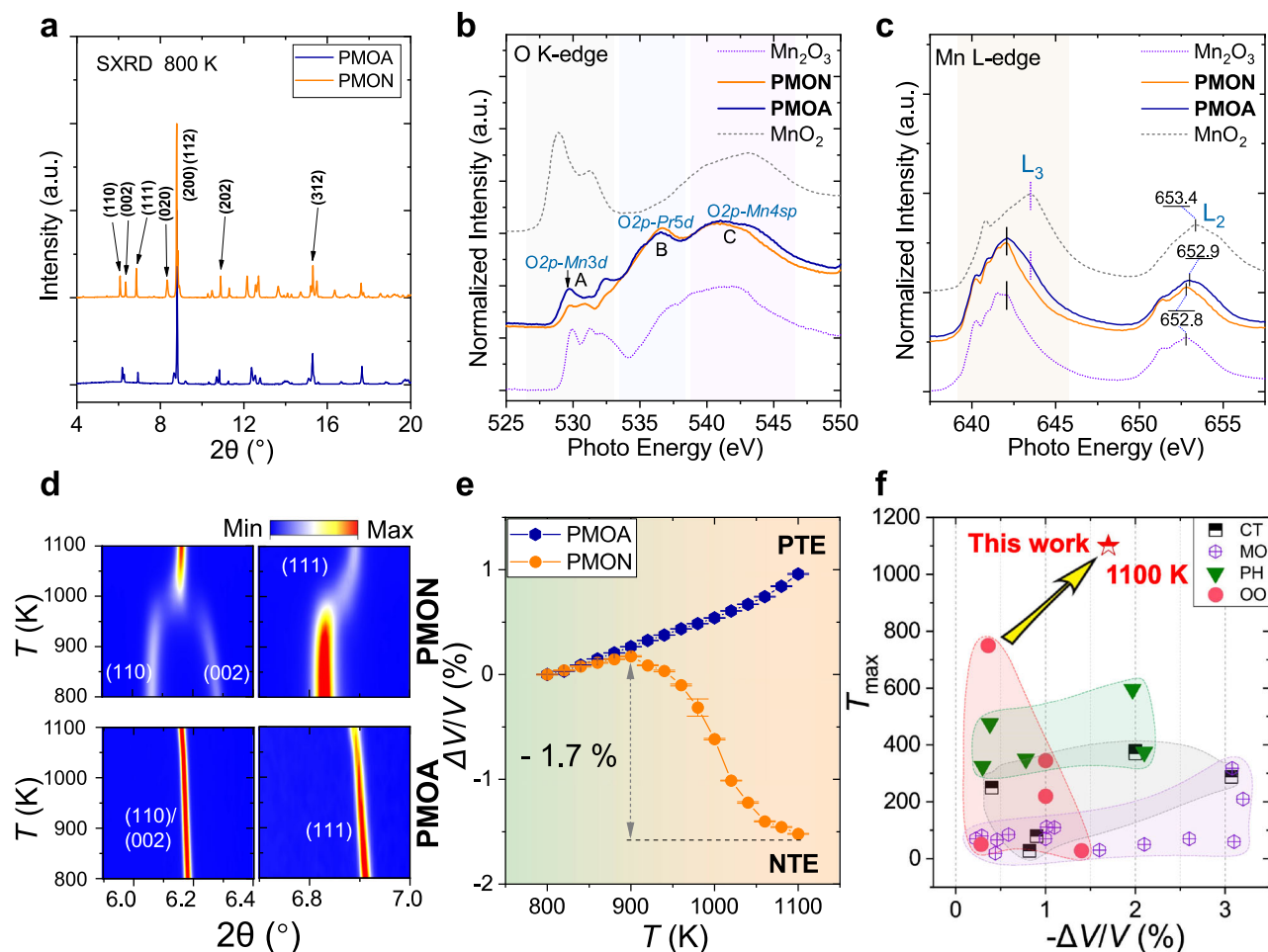


**Fig. 1 | Oxygen stoichiometry and thermal expansion in PMOA and PMON.**

**a** SXRD patterns of PMOA and PMON at 800 K with indexed diffraction peaks. **b** The O K-edge, and **(c)** Mn L-edge XAS spectrum of PMOA, PMON, reference samples ( $\text{Mn}_2\text{O}_3$ ,  $\text{MnO}_2$ ). **d** Contour plots of typical diffraction peaks (110)/(002) and (111) of PMOA and PMON. **e** The relative lattice volume change  $\Delta V/V$ , along with error bars from the standard error of lattice volumes. The green/orange colored

background represents a gradual change in temperature from low to high.

**f** The relative lattice volume shrinkage  $-\Delta V/V$  versus the maximum working temperature  $T_{\text{max}}$  of giant NTE materials induced by charge transfer (CT), magnetic order (MO), phonons (PH), and orbital ordering (OO). Detailed giant NTE data are listed in Table S1, Supplementary Information. Source data are provided as a Source Data file.

shifts in XAS spectra across beamlines. A detailed discussion of this phenomenon is provided in the text immediately following Fig. S10. Moreover, multiple batches of samples were synthesized, with XRD results demonstrating consistent lattice constants (Fig. S12, Table S2). We further characterized the magnetism, electrical resistance, and thermal conductivity of PMON and PMOA, as presented in Figs. S13–15.

### Structural evolution and JT distortion

As mentioned above, the progressive evolution of SXRD patterns (Fig. 1e, S2a–d) confirms PMON undergoes a structural phase transition near 1000 K, characterized by the coexistence of two orthorhombic  $Pnma$  phases (Phase1 and Phase2) above this temperature. Lattice contraction in PMON arises primarily from compression along the  $b$ -axis, while  $a$ - and  $b$ -dimensions converge in Phase2 to form a metrically quasi-tetragonal structure (Fig. S5d, e).

First, we focus on the JT distortion of  $\text{MnO}_6$  octahedra. Figure 2a illustrates the  $\text{MnO}_6$  octahedral substructure in PMON, annotated with critical bond lengths (longest  $d_l$ , intermediate  $d_m$ , shortest  $d_s$ ) and Mn–O–Mn bond angles ( $\gamma$ ,  $\beta$ ). Both PMOA and PMON exhibit significant  $d_l$ – $d_s$  disparities below 900 K (Fig. 2b, c), indicative of strong JT distortions. At 800 K, PMOA demonstrates  $d_l = 2.14 \text{ \AA}$  /  $d_s = 1.89 \text{ \AA}$  compared to PMON's  $d_l = 2.20 \text{ \AA}$  /  $d_s = 1.91 \text{ \AA}$ , with PMON displaying greater

JT distortion magnitude in this regime. Quantitative JT distortion analysis ( $\delta = [d_l - d_s] / [2(d_l + d_s)]$ ) reveals distinct thermal responses (Fig. 2f). PMOA maintains persistent distortion ( $\delta \approx 3.1\%$ ) up to 1100 K, while PMON shows dramatic  $\delta$  reduction from 3.5% at 900 K (Phase 1) to 1.4% at 920 K, stabilizing at ca. 1.1% in Phase 2 (920–1100 K).

Next, we focus on the relative distortion between the neighboring  $\text{MnO}_6$  octahedron, assessed by the bond angles  $\gamma$  and  $\beta$ . Bond angle evolution provides further mechanistic insight: PMOA retains constant  $\gamma$  and  $\beta$  values across temperatures (Fig. 2d), reflecting rigid octahedral connectivity. Conversely, PMON exhibits abrupt increases in  $\gamma$  and  $\beta$  at 920 K (Fig. 2e), signaling reduced octahedral tilting. This contrast suggests PMOA possesses “frozen”  $\text{MnO}_6$  octahedra, while PMON enables enhanced structural flexibility. Note that lattice contraction accompanied by increased octahedral rotational degree of freedom was previously observed in  $\text{LaMnO}_3$ <sup>31</sup>. The PMON volume contraction initiating at 900 K correlates with bond length convergence and planar octahedral alignment, marking an OO to OD transition between 900–920 K. In contrast, PMOA maintains strong JT distortions and preserved OO state across the whole temperature range.

### Local structure investigation

In addition to the average structural evolution through SXRD data refinement, we notice that local structural features, distinct from the

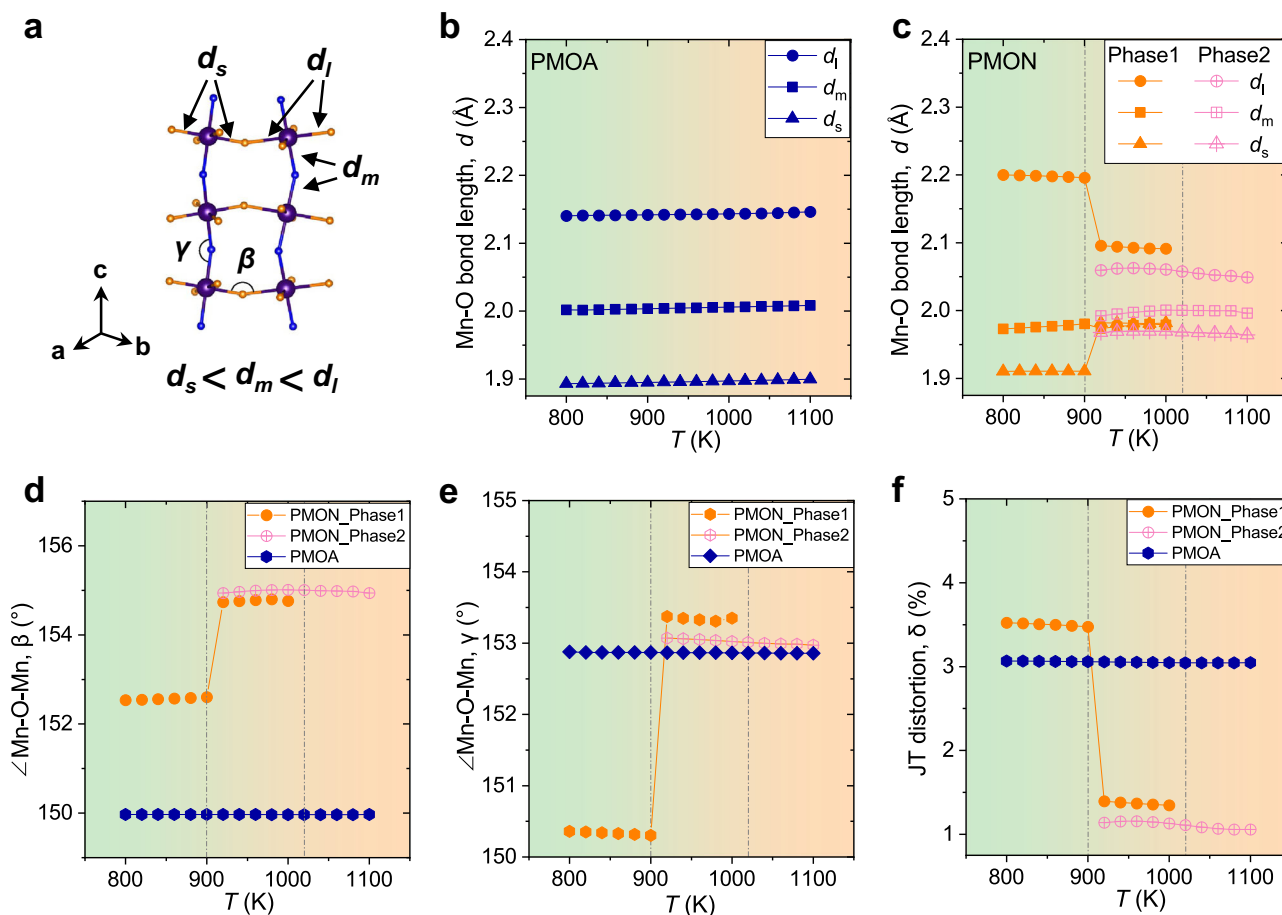


**Fig. 2 | Temperature-dependent lattice parameters and JT distortion.** **a** The substructure of an orthorhombic PMON with the longest, mediate, and shortest Mn-O bonds as indicated by  $d_l$ ,  $d_m$ , and  $d_s$ , respectively. The Mn-O-Mn bond angles are marked by  $\gamma$  and  $\beta$ . **b** The Mn-O-Mn bond lengths  $d_l$ ,  $d_m$ , and  $d_s$  of PMOA. **c** The Mn-O-Mn bond lengths of PMON (Phase1 and Phase2). **d** The Mn-O-Mn bond angles

$\beta$ . **e** The Mn-O-Mn bond angles  $\gamma$ . **f** JT distortion  $\delta$ . Phase 1 of PMON experienced a jump in  $\beta$  and  $\gamma$  and a sudden drop in  $\delta$  beyond 900 K. Mn atoms (large size) in purple, O atoms (small size) in blue/orange. The green/orange colored background represents a gradual change in temperature from low to high. Source data are provided as a Source Data file.

long-range periodic atomic arrangement, critically influence local electron and orbital configurations<sup>5,13,32,41,42</sup>. To elucidate these structural disparities between PMOA and PMON, synchrotron X-ray pair distribution function (PDF) analysis was implemented.

Initially, the average orthorhombic structural model (*Pnma* symmetry with constrained unit cell parameters and atomic positions) derived from SXR D Rietveld refinement was applied to fit the short-range PDF data (Fig. 3a, upper panel). The relatively poor fit quality ( $R_w = 28\%$ ) revealed significant local structural deviations from the average periodic structure, as evidenced by mismatches between experimental and calculated PDF profiles in the 1.5–6 Å r-range (indicated by red arrows). Subsequently, PDF refinement with relaxed *Pnma* symmetry constraints (unrestricted unit cell parameters and atomic positions) substantially improved the fit ( $R_w = 16.3\%$ , Fig. 3a middle panel), yielding a 2D model characterized by *ab*-plane confinement of the longest Mn-O bonds (Fig. 3d).

Ultimately, a monoclinic *P2<sub>1</sub>/c* symmetry model demonstrated superior PDF fitting ( $R_w = 10.5\%$ , Fig. 3a lower panel), revealing three-dimensional orientation of the longest Mn-O bonds rather than the planar restriction observed in the 2D model (as discussed later in the text). This energetically favorable 3D configuration exhibited enhanced agreement with experimental data, corroborated by minimized residual differences in  $\Delta G(r)$  profiles (purple curve, lower panel). These findings indicate a short-range symmetry breakdown in PMON from orthorhombic to monoclinic structure, highlighted by 3D-ordered Mn-O bond elongation. Contrastingly, in the case of PMOA, fits of *Pnma* and *P2<sub>1</sub>/c*

symmetry to the PDF data did not show a significant difference, suggesting no such symmetry breakdown occurred (Fig. S15).

In the PDF fitting of PMON, we can derive two types of models (2D and 3D models) with different arrangements of the longest Mn-O bonds. The 3D model's octahedral substructure reveals two distinct  $\text{MnO}_6$  units (royal/purple in Fig. 3b) with alternating corner connectivity. The longest Mn-O bond ( $d_1 = 2.24$  Å vs  $d_2 = 2.20$  Å) in the two different octahedra creates crosswise alignment in three-dimensional space (Fig. 3c). This contrasts sharply with the equatorial plane (*i.e.*, the *ab* plane) restriction observed in the 2D model (Fig. 3d). In PMOA, only a 2D model was derived, whether utilizing *Pnma* or *P2<sub>1</sub>/c* symmetries in the fitting (Fig. S15). This unique orbital configuration of PMON possibly enables the flexibility of  $\text{MnO}_6$  octahedra and facilitates OD through modified Mn-3d/O-2p hybridization, potentially correlating with the colossal NTE observed in PMON. The PDF fitting procedure is detailed in the Methods section. Theoretical investigations of orbital configuration-NTE relationships will be discussed later in the text.

#### Atomic-scale microstructure

To further elucidate the local atomic structure, we conducted atomic-resolution aberration-corrected scanning transmission electron microscopy (Cs-corrected STEM) studies. Figure 4a presents an annular bright-field (ABF) image of PMON along the [110] zone axis, and Fig. 4b displays its corresponding geometric phase analysis (GPA), revealing pronounced local strain field fluctuations. High-magnification high-angle annular dark-field (HAADF) imaging along

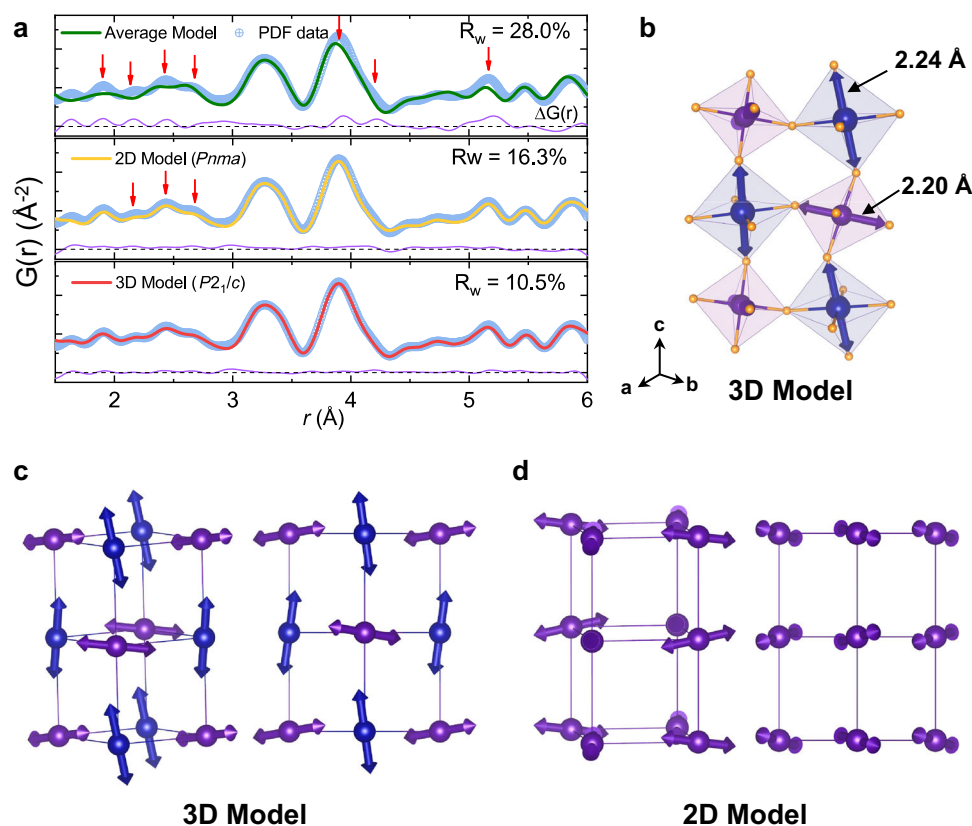


**Fig. 3 | Local structure investigation of PMON.** **a** Fit of three models to the PDF data by using (i) average structure model extracted from the SXRD Rietveld refinement (*Pnma* symmetry, green line), (ii) 2D model (*Pnma* symmetry, yellow line, discussed in the text), and (iii) 3D model (*P2<sub>1</sub>/c* symmetry, red line). The red arrows highlight the discrepancy between the experimental and calculated PDF( $\Delta G(r)$ ).  $R_w$  is the goodness of fit. **b** Substructure of 3D model. The longest Mn–O bonds in different  $MnO_6$  octahedra (Mn atoms in Royal and purple, O atoms

in orange) are shown by arrows. **c** Overall viewing of the longest Mn–O bond orientation in the 3D model. **d** The longest Mn–O bond orientation in the 2D model. Only Mn networks are presented. The longest Mn–O bonds of the 3D model are distributed in the horizontal and vertical planes. In contrast, the 2D model has the longest Mn–O bonds, approximately confined within the horizontal planes, *i.e.*, *ab* planes. Mn atoms in royal/purple, O atoms in orange. Source data are provided as a Source Data file.

[100] (Fig. 4c) resolves alternating Pr and Mn atomic columns, further corroborated by energy-dispersive spectroscopy (EDS) elemental mapping. Figures 4d, e compare cation ordering in PMON and PMOA, respectively. In PMON (Fig. 4d, e), HAADF and ABF imaging consistently reveal a zigzag (Z-shaped) cation arrangement. This configuration aligns with the 3D structural model derived from PDF refinement under *P2<sub>1</sub>/c* symmetry (Fig. 4h, left panel), contrasting sharply with the quasi-linear cation alignment predicted by the orthorhombic *Pnma* 2D model (Fig. 4h, right panel). The observed Z-type ordering directly validates the local symmetry reduction (orthorhombic to monoclinic) identified through PDF analysis. Concerning PMOA, both HAADF and ABF images show a quasi-linear cation arrangement (Fig. 4f, g), consistent with its 2D structural models refined under either *Pnma* or *P2<sub>1</sub>/c* symmetry (Fig. 4i). This structural invariance under differing symmetry constraints confirms the absence of significant local symmetry breaking in PMOA.

### Theoretical investigation

The JT distortion in  $MnO_6$  octahedra promotes preferential electron occupancy in the Mn *3d* orbitals, stabilizing OO. The reduction of JT distortion, concomitant with the onset of OD, triggers a redistribution of *3d* electrons, thereby inducing anisotropic Coulomb interactions across crystallographic directions<sup>41</sup>. This directional electronic reorganization drives lattice parameter adjustments and NTE. Unlike conventional NTE mechanisms involving low-frequency phonons or magnetic order, the dynamic evolution of JT distortion governs the

giant NTE observed in PMON. To elucidate the interplay between orbital configuration, JT distortion, and NTE, we performed density functional theory (DFT) calculations on PMON-derived structural models under varying conditions.

DFT simulations compared two PMON configurations: Structure I (room temperature, RT) and Structure II (high temperature, HT), both with constrained oxygen positions to preserve specific Mn–O bond distances and JT distortion. Figure 5a reveals alternating *3d* orbital patterns at neighboring Mn sites in Structure I, hallmarking robust OO. Conversely, Structure II (Fig. 5b) exhibits a distorted-cross orbital morphology indicative of OD. The observed orbital occupancy patterns at room temperature (RT) and high temperature (HT) accurately reflect the electronic configuration characteristics of PMON as it undergoes the critical transition from OO to OD. To probe defect-mediated orbital modulation, we constructed derivative models from Structure I: oxygen-unconstrained (III), single/double oxygen-intercalated (IV/V), and hole-doped (VI) systems. Structures III–V retained OO (Fig. 5c–e), mirroring experimental observations in oxygen-rich PMOA. Notably, only hole-doped Structure VI (Fig. 5f) exhibited OD, underscoring hole-doping-specific orbital destabilization.

OO is positively correlated with JT distortion magnitude (denoted as  $\delta$ , see Section 3.1). A large  $\delta$  value indicates significant disparities in Mn–O bond lengths and preferential electron occupancy in the *3d* orbitals. Conversely, a smaller  $\delta$  value suggests more uniform Mn–O bond lengths and a randomized *3d* electron distribution. Figure 5g

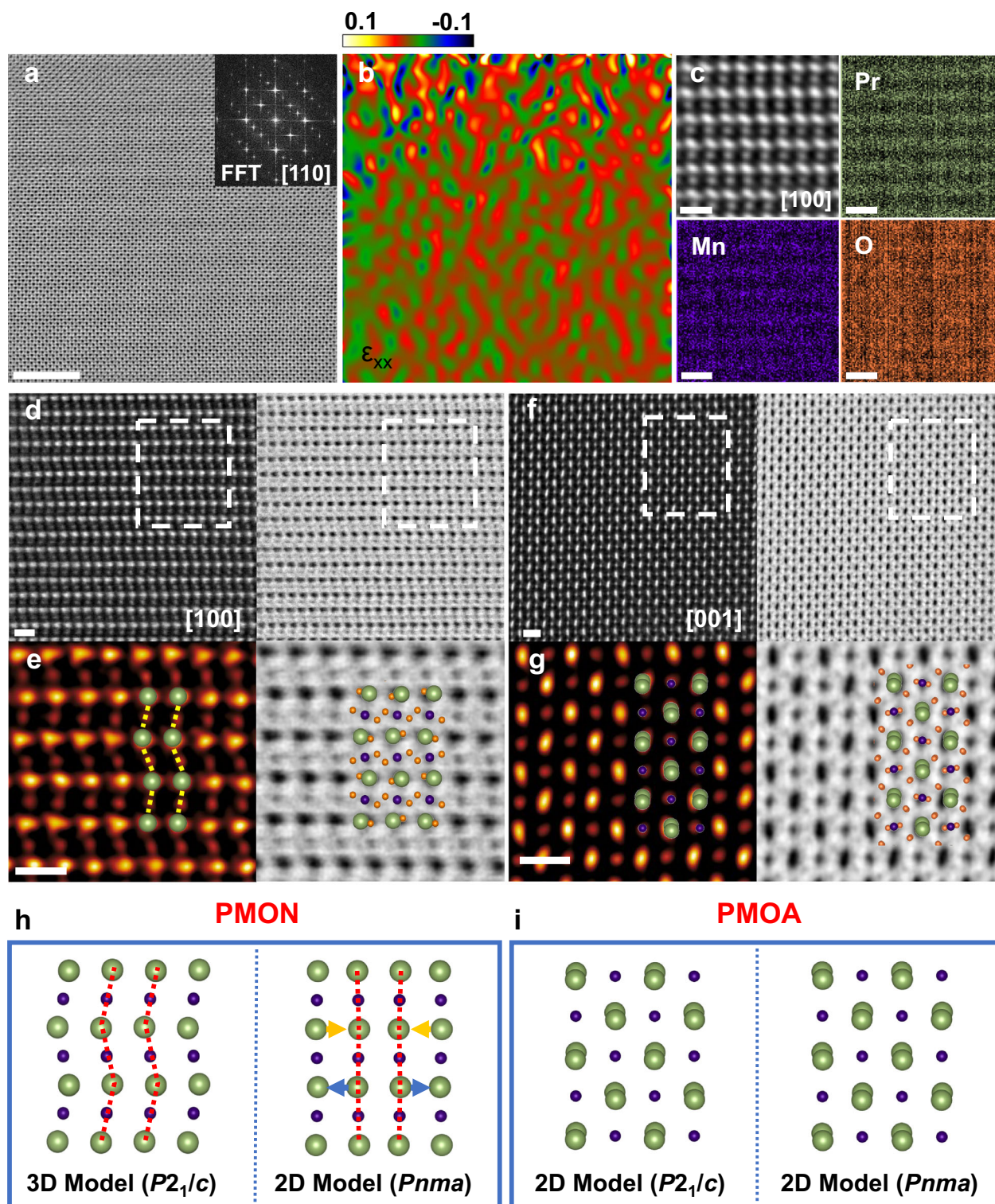


**Fig. 4 | Atomic structure analysis in PMOA and PMON.** **a** Atomic-resolution STEM-ABF image of PMON along [110] zone axis with FFT image inset. **b** The corresponding GPA strain analysis of (a) using 200 and 0–20 reflections. **c** The STEM-HAADF image and atomic EDS mapping of PMON along [100] zone axis. The HAADF and ABF images of (d) PMON along [100] zone axis, and (f) of PMOA along [001], respectively. **e, g** Enlarged images of the white-rectangle regions in (d) and (f) show the cation (Pr and Mn) network arrangements. **h, i** Structural models derived from PDF fit of PMON and PMOA. The yellow and

blue arrows indicate the slight static movements of Pr atoms. For PMON, the cation network in (e) shows a zigzag arrangement, consistent with the 3D model shown in (h). Meanwhile, the quasi-linear cation arrangement in the 2D model ((h), right panel) is inconsistent with the experimental image of (e). Regarding PMOA, only the 2D model could be generated, whether using  $P2_1/c$  or  $Pnma$ . This 2D model agrees with the atomic arrangement in (g). The scale bar in (a) indicates 5 nm, and the other scale bars indicate 0.5 nm. Pr atoms in green, Mn atoms in purple, O atoms in orange.

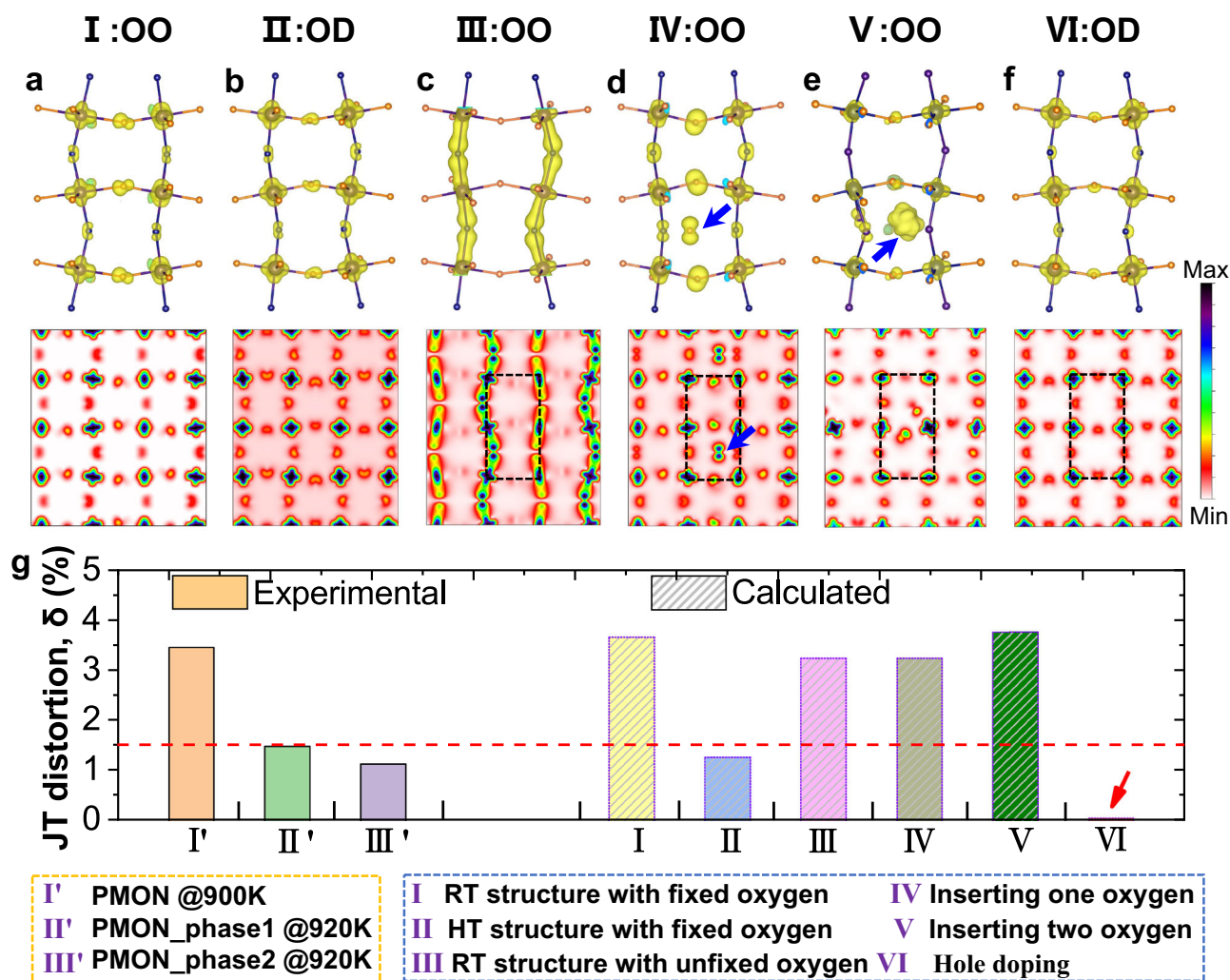


**Fig. 5 | Partial charge density (PCD) and JT distortion of PMON structures.** **a–f** PCD (upper panel) and PCD map projected along [100] direction (lower panel) of structure I–VI: **a**, **b** I and II structures with fixed oxygen at room temperature (RT) and high temperature (HT); **c** III: RT structure with unfixed oxygen; **d** IV: structure with inserting one oxygen; **e** V: structure with inserting two oxygens; **f** VI: structures with hole doping. The blue arrow indicates the existence of interstitial oxygen.

Scale bar: charge intensity. **g** A summary of JT distortion,  $\delta$ . Experimental  $\delta$  derives from structures I'–III' of PMON at 900 K and 920 K. Calculated  $\delta$  is extracted based on the calculated structures I–VI of PMON. The red dashed line represents the threshold value of  $\delta$ , below which the specific structural configurations exhibit OD. Source data are provided as a Source Data file.

summarizes the JT distortion derived from both experimental and calculated structures. Experimental PMON data at 900 K ( $\delta = 3.47\%$ , Structure I') confirm OO dominance, while HT phases at 920 K (Structures II'/III':  $\delta = 1.50\% / 1.14\%$ ) reflect OD onset, coinciding with NTE emergence. This suggests that changes in 3d electron occupancy, closely linked to Coulomb forces in different directions, drive the anomalous lattice volume changes with temperature. In addition, calculated Structure I (RT, fixed oxygen) yielded  $\delta = 3.68\%$  (OO), whereas Structure II (HT, fixed oxygen) showed  $\delta = 1.28\%$  (OD). Oxygen-intercalated models to mimic PMOA (Structure IV/V,  $\delta > 3\%$ ) maintained OO. This indicates that interstitial oxygen insertion in  $\text{PrMnO}_3$  does not disrupt the OO state, contrasting with the interstitial-oxygen-driven OO destabilization found in  $\text{Ca}_2\text{RuO}_4$ <sup>11</sup>. Strikingly, hole doping (Structure VI) minimized  $\delta$  to 0.06% (OD, Fig. 5g), highlighting its possibility to affect the preferred occupancy of 3d electrons.

In conclusion, we present, to the best of our knowledge, the first observation of giant NTE exceeding 1000 K ( $\alpha_V = -85 \times 10^{-6} \text{K}^{-1}$ , 900–1100 K) in PMON, with a peak  $\alpha_V = -114 \times 10^{-6} \text{K}^{-1}$ , representing the highest operational temperature range among known giant NTE materials. Intriguingly, oxygen-rich PMOA shows a complete suppression of NTE behavior and instead transitions to conventional

PTE. Comprehensive structural analysis indicates that the anomalous NTE occurs along with the temperature-dependent evolution of JT distortions in  $\text{MnO}_6$  octahedra and an OO to OD transition. Notably, a local structural distortion characterized by 3D cross-arranged Mn–O bond elongation was identified in PMON through PDF analysis, in contrast to the 2D planar configurations observed in PMOA. This 3D structural motif is further confirmed by Cs-corrected high-resolution TEM imaging, which reveals characteristic zigzag alignments of Pr atomic columns. First-principles calculations provide direct evidence of oxygen-stabilized OO and demonstrate that hole doping effectively induces OD. These findings broaden the scope of high-temperature giant NTE materials characterized by unique local structural distortions, atomic configurations, and OD phenomena, offering potential applications for engineering components in operation.

## Methods

### Materials synthesis

$\text{Pr}_6\text{O}_{11}$  (99.99%, Macklin),  $\text{Mn}_2\text{O}_3$  (99.9%, Aladdin),  $\text{HNO}_3$  (65–68%, Sinopharm), and citric acid (> 99.5%, Aladdin) were used as starting materials. The PMOA containing excess oxygen was prepared using

the solid-state reaction method, which involves carefully mixing and grinding the  $\text{Pr}_6\text{O}_{11}$  and  $\text{Mn}_2\text{O}_3$  according to the nominal stoichiometric ratio. The mixed powder was annealed in the atmosphere at 1200 °C for 12 h. The PMON was prepared by a citrate decomposition method. Specifically, the  $\text{Pr}_6\text{O}_{11}$  and  $\text{Mn}_2\text{O}_3$  with a nominal stoichiometric ratio were dissolved in citrate and nitrate solutions, followed by evaporation at 120 °C and decomposed at 200 °C, leading to a fragile precursor. The precursor was ground into powder and annealed at 700 °C for 12 h in air to remove the organics and nitrates, and loaded into the tube furnace and heated at a ramping rate of 5 °C  $\text{min}^{-1}$  to 1100 °C, held at this temperature point for 12 h, and subsequently cooled in the furnace. The entire process was under the protection of high-purity nitrogen (99.99%) gas with a flow rate of 50 mL  $\text{min}^{-1}$ .

### SXRD, total scattering and XRD

Synchrotron X-ray experiments were conducted at the 11-ID-C and 17BM beamlines of Argonne National Laboratory. PMON and PMOA powders were loaded into Hilgenberg quartz glass capillaries within a glove box maintained at  $\text{O}_2$  and  $\text{H}_2\text{O}$  levels below 0.1 ppm. After temporary sealing with plasticine, the capillaries were sealed using a hydrogen pilot flame to preserve the sample under inert conditions. These sealed capillaries were then subjected to high-temperature X-ray measurements in transmission mode. Prior to heating, careful temperature calibration was performed. For heating, hot air was applied to the capillaries, with measurement parameters set as follows: exposure time at 90 s, waiting time at 120 s, and ramping rate at 20 K  $\text{min}^{-1}$ .

Synchrotron X-ray total scattering measurements were conducted by positioning the detector approximately 350 mm from the sample. Powder samples were sealed into 2 cm-long, 1 mm-diameter Kapton tubes, with both ends secured using plasticine. For data acquisition, the exposure time was set to 4 s per frame, with 30 consecutive frames collected to generate a single data image. To enhance data quality, twenty such data images were acquired and averaged. Prior to sample measurement, an empty Kapton tube was measured to record the background scattering signal. Total scattering data were processed using PDFgetx2, which involved corrections, background subtraction, and  $S(Q)$  normalization to yield high-quality structural information<sup>43</sup>.

High-temperature XRD patterns were acquired using a Rigaku powder X-ray diffractometer equipped with a Cu target, operating at 40 kV and 40 mA. Powder samples were uniformly dispersed on the Pt pad and transferred into the measurement chamber under vacuum conditions. The exposure time, wait time, and ramping rate were set to 45 min, 30 min and 10 K  $\text{min}^{-1}$ , respectively.

### XAS measurements

XAS for the O K-, Mn L-, and Mn K-edges were collected at multiple synchrotron facilities, including BL08U1A and BL14W1 of the Shanghai Synchrotron Radiation Facility (SSRF), as well as ID07 and ID46 of the High Energy Photon Source (HEPS). For the Mn L- and O K-edge measurements, samples were analyzed in total electron yield mode under high-vacuum conditions. To acquire high-quality Mn K-edge data, suitable amounts of samples were first mixed and ground with boron nitride powder, then pressed into 1 mm-thick pellets. Transmission mode was employed for data collection to ensure an edge jump of approximately 1, optimizing the signal-to-noise ratio for accurate spectral analysis.

### PDF analysis

The PDF  $G(r)$  function was refined using the small-box method in PDFgui<sup>44</sup> with a  $Q$  resolution of 25  $\text{\AA}^{-1}$ . Structural models were constructed based on  $Pnma$  and  $P2_1/c$  space groups. Initial parameters for the average structural model were sourced directly from Rietveld

refinement of the SXRD patterns. For both 2D and 3D models, refinement included variable parameters such as scale factors,  $\delta_i$ ,  $Q_{\text{broad}}$ ,  $Q_{\text{damp}}$ , atomic coordinates, and isotropic atomic displacement parameters (ADPs). The starting value of  $Q_{\text{damp}}$  was set to 0.03, which was determined by calibration of the  $\text{CeO}_2$  reference sample. In the 3D model based on  $P2_1/c$  symmetry, the  $\alpha$  angle was allowed to relax. Additionally, the ADPs of O1 and O2 in the 3D model were constrained to be equivalent, ensuring consistency in the number of refined parameters with the 2D model. Notably, the  $P2_1/c$  symmetry introduces two distinct O2 sites (O2 and O2'), but to avoid unnecessary parameter expansion, the symmetry relationship between O2 ( $x, y, z$ ) and O2' ( $1-x, y+0.5, z$ ) was enforced. Both PMON and PMOA were refined against both 2D and 3D models. For PMON, the 3D model yielded a significantly better fit ( $R_w = 10.5\%$ ) compared to the 2D model ( $R_w = 16.3\%$ ), whereas for PMOA, the fits of the 3D and 2D models were highly comparable. This discrepancy underscores the presence of local structural distortions in PMON, characterized by 3D-ordered Mn-O bond elongation.

### Cs-corrected STEM measurements

The high-angle annular dark-field aberration-correlated scanning transmission electron microscopy (HAADF-STEM, Titan 80–300 FEI) was employed to study the atomic structure of  $\text{PrMnO}_3$ . The specimen was cut finely by a focused ion beam (FIB) method (Helios 450, FEI).

### DFT calculations

The first-principles density functional theory (DFT) calculations were employed by the Vienna Ab initio Simulation Package (VASP)<sup>45,46</sup>. The exchange-correlation functional was selected to be the revised Perdew-Burke-Ernzerhof variant for solids (PBEsol) of the generalized gradient approximation (GGA)<sup>47</sup>. The plane wave basis set and a cutoff energy of 450 eV. The electronic and force convergence criteria were chosen as  $10^{-5}$  eV and  $10^{-3}$  eV  $\text{\AA}^{-1}$ , respectively. To identify the partial charge density and density of states in PMON which was inserted into two oxygens, a  $2 \times 2 \times 1$  supercell was constructed. The Brillouin zone was sampled using a  $6 \times 6 \times 4$  and  $3 \times 3 \times 4$  Gamma mesh for the PMON, and PMON inserted two oxygens. The spin polarization of Pr was taken into consideration by setting the ferromagnetic order according to the previously reported magnetic geometry<sup>48</sup>. The effect of electronic corrections on the Pr 4f shell was considered using the GGA+ $U$  method with  $U = 7.0$  eV and  $J = 7.0$  eV (for Pr), and  $U = 4.0$  eV,  $J = 0.87$  eV for the 3d orbital of the Mn<sup>49</sup>.

### Data availability

The data supporting the findings of this study are available from the article and the supplementary materials file. All the raw data are available from the corresponding authors upon request. Source data are provided with this paper.

### References

1. Takenaka, K. Negative thermal expansion materials: technological key for control of thermal expansion. *Sci. Technol. Adv. Mat.* **13**, 11 (2012).
2. Zhang, Y. et al. Thermal-expansion offset for high-performance fuel cell cathodes. *Nature* **591**, 246–251 (2021).
3. Mary, T. A., Evans, J. S. O., Vogt, T. & Sleight, A. W. Negative thermal expansion from 0.3 to 1050 Kelvin in  $\text{ZrW}_2\text{O}_8$ . *Science* **272**, 90–92 (1996).
4. Greve, B. K. et al. Pronounced negative thermal expansion from a simple structure: cubic  $\text{ScF}_3$ . *J. Am. Chem. Soc.* **132**, 15496–15498 (2010).
5. Hu, L. et al. Localized symmetry breaking for tuning thermal expansion in  $\text{ScF}_3$  nanoscale frameworks. *J. Am. Chem. Soc.* **140**, 4477–4480 (2018).

6. Song, Y. Z. et al. Zero thermal expansion in magnetic and metallic Tb(Co,Fe)<sub>2</sub> intermetallic compounds. *J. Am. Chem. Soc.* **140**, 602–605 (2018).
7. Huang, R. J. et al. Giant negative thermal expansion in NaZn<sub>13</sub>-type La(Fe, Si, Co)<sub>13</sub> compounds. *J. Am. Chem. Soc.* **135**, 11469–11472 (2013).
8. Azuma, M. et al. Colossal negative thermal expansion in BiNiO<sub>3</sub> induced by intermetallic charge transfer. *Nat. Commun.* **2**, 347 (2011).
9. Takenaka, K., Okamoto, Y., Shinoda, T., Katayama, N. & Sakai, Y. Colossal negative thermal expansion in reduced layered ruthenate. *Nat. Commun.* **8**, 14102 (2017).
10. Pachoud, E., Cumby, J., Lithgow, C. T. & Attfield, J. P. Charge order and negative thermal expansion in V<sub>2</sub>OPO<sub>4</sub>. *J. Am. Chem. Soc.* **140**, 636–641 (2018).
11. Hu, L. et al. Origin and absence of giant negative thermal expansion in reduced and oxidized Ca<sub>2</sub>RuO<sub>4</sub>. *Chem. Mater.* **33**, 7665–7674 (2021).
12. Agne MT, Anand S, Snyder GJ. Inherent anharmonicity of harmonic solids. *Research-China* **2022**, (2022).
13. Iikubo, S. et al. Local lattice distortion in the giant negative thermal expansion material Mn<sub>3</sub>Cu<sub>1-x</sub>Ge<sub>x</sub>N. *Phys. Rev. Lett.* **101**, 205901 (2008).
14. Zheng, X. G. et al. Giant negative thermal expansion in magnetic nanocrystals. *Nat. Nanotechnol.* **3**, 724–726 (2008).
15. Gao, Q. L. et al. Switching between giant positive and negative thermal expansions of a YFe(CN)<sub>6</sub>-based prussian blue analogue induced by guest species. *Angew. Chem. Int Ed.* **56**, 9023–9028 (2017).
16. Sun, H. Y. et al. Colossal anisotropic thermal expansion through coupling spin crossover and rhombus deformation in a hexanuclear {Fe<sup>III</sup>4Fe<sup>II</sup>2} compound. *Angew. Chem. Int Ed.* **62**, 8 (2023).
17. Xu, M. et al. Giant uniaxial negative thermal expansion in FeZr alloy over a wide temperature range. *Nat. Commun.* **14**, 4439 (2023).
18. Mazzone, D. G. et al. Kondo-induced giant isotropic negative thermal expansion. *Phys. Rev. Lett.* **124**, 125701 (2020).
19. Yamamoto, H., Imai, T., Sakai, Y. & Azuma, M. Colossal negative thermal expansion in electron-doped PbVO<sub>3</sub> perovskites. *Angew. Chem. Int Ed.* **57**, 8170–8173 (2018).
20. Zhao, Y. Y. et al. Giant negative thermal expansion in bonded MnCoGe-based compounds with Ni<sub>2</sub>In-type hexagonal structure. *J. Am. Chem. Soc.* **137**, 1746–1749 (2015).
21. Lin, J. C. et al. Giant room-temperature barocaloric effect at the electronic phase transition in Ni<sub>1-x</sub>Fe<sub>x</sub>S. *Mater. Horiz.* **7**, 2690–2695 (2020).
22. Yu, C. Y. et al. An isotropic zero thermal expansion alloy with super-high toughness. *Nat. Commun.* **15**, 2252 (2024).
23. Cao, Y. L. et al. Ultrawide Temperature Range Super-Invar Behavior of R<sub>2</sub>(Fe,Co)<sub>17</sub> Materials (R = Rare Earth). *Phys. Rev. Lett.* **127**, 055501 (2021).
24. Liang, Z. L. et al. Uniaxial Negative Thermal Expansion in γ-LiBO with a Closed-Framework Diamond-Like Structure. *Chem. Mater.* **36**, 7299–7305 (2024).
25. Gao, Q. L. et al. Giant Negative Thermal Expansion in Ultralight NaB(CN)<sub>4</sub>. *Angew. Chem. Int Ed.* **63**, 6 (2024).
26. Spaldin, N. A. & Ramesh, R. Advances in magnetoelectric multiferroics. *Nat. Mater.* **18**, 203–212 (2019).
27. Tokura, Y. & Nagaosa, N. Orbital physics in transition-metal oxides. *Science* **288**, 462–468 (2000).
28. Mefford, J. T., Hardin, W. G., Dai, S., Johnston, K. P. & Stevenson, K. J. Anion charge storage through oxygen intercalation in LaMnO perovskite pseudocapacitor electrodes. *Nat. Mater.* **13**, 726–732 (2014).
29. Suntivich, J. et al. Design principles for oxygen-reduction activity on perovskite oxide catalysts for fuel cells and metal-air batteries. *Nat. Chem.* **3**, 546–550 (2011).
30. Uehara, M., Mori, S., Chen, C. H. & Cheong, S. W. Percolative phase separation underlies colossal magnetoresistance in mixed-valent manganites. *Nature* **399**, 560–563 (1999).
31. Qiu, X. Y., Proffen, T., Mitchell, J. F. & Billinge, S. J. L. Orbital correlations in the pseudocubic and rhombohedral phases of LaMnO<sub>3</sub>. *Phys. Rev. Lett.* **94**, 177203 (2005).
32. Thygesen, P. M. M. et al. Local structure study of the orbital order/disorder transition in LaMnO<sub>3</sub>. *Phys. Rev. B* **95**, 174107 (2017).
33. Sánchez, M. C., Subías, G., García, J. & Blasco, J. Cooperative Jahn-Teller phase transition in LaMnO<sub>3</sub> studied by X-ray absorption spectroscopy. *Phys. Rev. Lett.* **90**, 045503 (2003).
34. Chatterji, T., Fauth, F., Ouladdiaf, B., Mandal, P. & Ghosh, B. Volume collapse in LaMnO<sub>3</sub> caused by an orbital order-disorder transition. *Phys. Rev. B* **68**, 052406 (2003).
35. Tikkanen, J., Kauhala, S., Huhtinen, H. & Paturi, P. Anomalous thermal expansion in (Pr, Ca)MnO<sub>3</sub> due to orbital ordering. *Physcs Proc.* **75**, 475–481 (2015).
36. Sánchez D, Alonso JA, Martínez-Lope MJ. Neutron-diffraction study of the Jahn-Teller transition in PrMnO<sub>3</sub>. *J. Chem. Soc. Dalton*, 4422–4425 (2002).
37. Vedmid', L. B., Yankin, A. M., Fedorova, O. M. & Kozin, V. M. Phase diagram of the Pr-Mn-O system in composition-temperature-oxygen pressure coordinates. *Russ. J. Phys. Chem.* **90**, 977–982 (2016).
38. Ulyanov, A. N. et al. Electron structure and magnetic properties of self-doped Pr<sub>1-x</sub>MnO<sub>3+δ</sub> manganites: XANES and EXAFS study. Comparing with A- and B-site doped perovskites. *Solid State Sci.* **118**, 106653 (2021).
39. Frati, F., Hunault, M. O. J. Y. & de Groot, F. M. F. Oxygen K-edge X-ray absorption spectra. *Chem. Rev.* **120**, 4056–4110 (2020).
40. Abbate, M. et al. Controlled-valence properties of La<sub>1-x</sub>Sr<sub>x</sub>FeO<sub>3</sub> and La<sub>1-x</sub>Sr<sub>x</sub>MnO<sub>3</sub> studied by soft-X-ray absorption spectroscopy. *Phys. Rev. B* **46**, 4511–4519 (1992).
41. Cao, D., Bridges, F., Kowach, G. R. & Ramirez, A. P. Correlated atomic motions in the negative thermal expansion material ZrW<sub>2</sub>O<sub>8</sub>: a local structure study. *Phys. Rev. B* **68**, 014303 (2003).
42. Qin, F. Y. et al. Integrating abnormal thermal expansion and ultra-low thermal conductivity into (Cd,Ni)<sub>2</sub>Re<sub>2</sub>O<sub>7</sub> via synergy of local structure distortion and soft acoustic phonons. *Acta Mater.* **264**, 119544 (2024).
43. Qiu, X., Thompson, J. W. & Billinge, S. J. PDFgetX2: a GUI-driven Program to Obtain the Pair Distribution Function from X-ray Powder Diffraction Data. *J. Appl. Crystallogr.* **37**, 678 (2004).
44. Farrow, C. L. et al. PDFfit2 and PDFgui: computer programs for studying nanostructure in crystals. *J. Phys.-Condens Mat.* **19**, 335219 (2007).
45. Kresse, G. & Furthmüller, J. Efficiency of ab-initio total energy calculations for metals and semiconductors using a plane-wave basis set. *Comput. Mater. Sci.* **6**, 15–50 (1996).
46. Kresse, G. & Furthmüller, J. Efficient iterative schemes for ab initio total-energy calculations using a plane-wave basis set. *Phys. Rev. B* **54**, 11169–11186 (1996).
47. Perdew, J. P. et al. Restoring the density-gradient expansion for exchange in solids and surfaces. *Phys. Rev. Lett.* **100**, 136406 (2008).
48. Mishra, S. K., Gupta, M. K., Mittal, R., Kolesnikov, A. I. & Chaplot, S. L. Spin-phonon coupling and high-pressure phase transitions of RMnO<sub>3</sub> (R = Ca and Pr): An inelastic neutron scattering and first-principles study. *Phys. Rev. B* **93**, 214306 (2016).
49. Bouadjemi, B., Bentata, S., Abbad, A., Benstaali, W. & Bouhafs, B. Half-metallic ferromagnetism in PrMnO<sub>3</sub> perovskite from first principles calculations. *Solid State Commun.* **168**, 6–10 (2013).

## Acknowledgments

We acknowledge funding from Science Fund Program for Distinguished Young Scholars (Overseas), National Natural Science Foundation of China (No. 22205171, 52472076, 22405202), Key Research and Development Program of Shaanxi Province (No. 2024CY2-GJHX-86 and 2024PT-ZCK-41), International Postdoctoral Exchange Fellowship Program (Talent-Introduction Program), China Postdoctoral Science Foundation (No. 2023M732754), Postdoctoral Research Project of Shaanxi Province (No. 3127100000040), and Natural Science Basic Research Program General Project–Youth Project of Shaanxi Province (2024JC-YBQN-0117).

## Author contributions

L.H. and F.Q. conceived the idea of the work. F.Q. carried out the main experiments, data processed, and prepared the manuscript. P.C., D.W., X.B., Y.F., J.W., and P.Z. carried out the measurement and contributed to calculations. L. H., X. D., and J.S. supervised the project. All the authors discussed the results and commented on the manuscript.

## Competing interests

The authors declare no competing interests.

## Additional information

**Supplementary information** The online version contains supplementary material available at <https://doi.org/10.1038/s41467-025-64925-7>.

**Correspondence** and requests for materials should be addressed to Feiyu Qin, Pengtao Cheng or Lei Hu.

**Peer review information** *Nature Communications* thanks the anonymous reviewers for their contribution to the peer review of this work. A peer review file is available.

**Reprints and permissions information** is available at <http://www.nature.com/reprints>

**Publisher's note** Springer Nature remains neutral with regard to jurisdictional claims in published maps and institutional affiliations.

**Open Access** This article is licensed under a Creative Commons Attribution-NonCommercial-NoDerivatives 4.0 International License, which permits any non-commercial use, sharing, distribution and reproduction in any medium or format, as long as you give appropriate credit to the original author(s) and the source, provide a link to the Creative Commons licence, and indicate if you modified the licensed material. You do not have permission under this licence to share adapted material derived from this article or parts of it. The images or other third party material in this article are included in the article's Creative Commons licence, unless indicated otherwise in a credit line to the material. If material is not included in the article's Creative Commons licence and your intended use is not permitted by statutory regulation or exceeds the permitted use, you will need to obtain permission directly from the copyright holder. To view a copy of this licence, visit <http://creativecommons.org/licenses/by-nc-nd/4.0/>.

© The Author(s) 2025